Low Reynolds Number Effect on Energy Extraction Performance of Semi-Passive Flapping Foil

A. Javed[1†], K. Djidjeli[2], A. Naveed[1], and J. T. Xing[2]

[1] *College of Aeronautical Engineering, National University of Sciences and Technology, Pakistan*
[2] *Faculty of Engineering and Environment, University of Southampton, UK*

† *Corresponding Author Email*: *ali.javed@cae.nust.edu.pk*

ABSTRACT

In this paper, 2-D numerical solution scheme is used to study the performance of semi-passive flapping foil flow energy harvester at Reynolds numbers ranging from 5000 to 50,000. The energy harvester comprises of NACA0015 airfoil which is supported on a translational spring and damper. An external sinosoidal pitch excitation is provided to the airfoil. Energy is extracted from the flow induced vibration of airfoil in translational mode. Movement of airfoil is accommodated in fluid domain by using a hybrid meshfree-Cartesian fluid grid. A body conformal meshfree nodal cloud forms the near field domain, encompassing the airfoil. During the simulation, the solid boundary causes the motion of the meshfree nodal cloud, without necessitating re-meshing. In the far field, the static Cartesian grid encloses and partly overlaps the meshfree nodal cloud. A coupled mesh based and meshfree solution scheme is utilized to solve laminar flow, viscous, incompressible equations, in Arbitrary-Lagrangian-Eulerian (ALE) formulation, over a hybrid grid. Spatial discretization of flow equations is carried out using radial basis function in finite difference mode (RBF-FD) over meshfree nodes and conventional finite differencing over Cartesian grid. Stabilized flow momentum equations are used to avoid spurious fluctuations at high Reynolds numbers. A closely coupled, partitioned, sub iteration method is used for fluid structure interaction. The study is focused to analyse the behaviour of flow energy harvesters at various Reynolds numbers. Effects of changing the translational spring stiffness and pitch activation frequency are also investigated. Instantaneous flow structures around the airfoil have been compared at different Reynolds numbers and pitch amplitudes. It is found that net power extracted by the system increases at high Reynolds numbers. Moreover, re-attachment of leading edge separation vortex plays an important role in ther overall system performance.

Keywords: Energy Harvesting, Fluid Structure Interaction, Semi-Passive Flow Energy Harvester, Hybrid grid, Meshfree Methods, RBF-FD.

NOMENCLATURE

θ	Pitch angle	F_y	Y component of the force acting on the lower side
θ_0	Pitch amplitude		
f	Pitch frequency	C_{op}	Coefficient of power
m	Solid mass	P	Extracted power
k	Spring stiffness	Re	Flow Reynolds number
b	Damping coefficient	η	Power extraction efficiency
c	chord	$\mathbf{u}$	Velocity of fluid
U	Free stream velocity	Pe	Peclet Number
F_x	X component of the resultant pressure force	Ω	Domain

1. INTRODUCTION

Energy extraction from wind and water currents has traditionally been achieved using rotary turbines. Extensive work has been done on design and development of such devices. However, this conventional design approach possesses some inherent limitations. For example, rotary blades produce high centrifugal stresses which necessitate the use of substantially strong and light materials. In case of large blades, high rotational speeds may have environmental concerns due to noise pollution and being dangerous to wildlife. Efficiency and applicability of rotary turbines are also subdued in shallow water due to limitations on the diameter which can be accommodated in the channel.

In recent years, flapping foil flow energy harvesters have evolved as a novel design concept. Originally it was opined that flapping foil is capable of

extracting energy only from wavy (unsteady) flow (Wu (1972),Wu and Chwang (1975)). However, later McKinney and DeLaurier (1981) coined the idea of 'wingmill'. In that, they proposed the use of flapping foil for extracting energy from incoming uniform flow. Since then, use of flapping foil has been investigated for flow energy harvesting by many researchers (Jones and Platzer (1997), Kinsey and Dumas (2008), Zhu and Peng (2009), Peng and Zhu (2009), Deng et al. (2015), Zhu (2012), Boragno et al. (2012)).

Flapping foil energy harvesters can be categorized into three major types on the basis of their activation modes. First category refers to the fully active mode in which the motion of flapping foil is prescribed along pitching as well as heaving axes. Significant work has been done in the past to understand the behaviour of such mechanisms (McKinney and DeLaurier (1981), Kinsey and Dumas (2008), Ashraf et al. (2011), Zhu (2011)). For example, Kinsey and Dumas (2008) carried out a parametric study for a range of pitch frequencies and pitch amplitudes. They suggested that carefully tuned parameters, for such systems, can result in net power extracted from the flow. Later, Ashraf et al. (2011) extended this investigation for two flapping foils in tandem. They investigated an optimal distance and phase difference between the two foils to maximize the energy extraction. Second type is the semi-passive mode in which energy is extracted through the coupling of flow induced as well as externally activated modes of oscillation (Zhu et al. (2009), Deng et al. (2015), Wu et al. (2014), Zhu and Peng (2009), Wu et al. (2015)). A typical model of the same method in a completely meshed domain can also be envisaged in the research carried out by Mirzaii and Passandideh-Fard (2012). For such systems, pitch mode of oscillation is generally activated by an external drive which produces time varying aerodynamic forces on the foil. As a result, the foil undergoes heaving oscillations which may be used for energy extraction. Zhu et al. (2009) studied the performance of semi-passive systems using 2D thin plate model and 3D non-linear boundary element methods. They examined that the performance of such systems could be enhanced by the presence of a solid wall in the vicinity of foil or by increasing the thickness of foil. Later, Wu et al. (2014) carried out a detailed investigation of wall effects on energy extraction performance. Zhu and Peng (2009) examined the vorticity control mechanism around the foil. They proposed that energy harvesting capacity could be increased if leading edge vortex is partially recovered after being detached from the airfoil. Wu et al. (2015) investigated the effects of adding a rigid or flexible flat trailing edge flap

to increase the net power extraction. Deng et al. (2015) studied the inertial effects on semi-passive foil energy harvesters. Third category is the fully passive mode in which the foil moves entirely under the influence of fluid forces without any external activation. In some cases, one mode of vibration is constrained to the other through mechanical linkages. For example, Young et al. (2013) proposed a flywheel and linkage mechanism to constraint the pitching motion of foil with heave motion. They observed that controlling the timing and location of leading edge vortex and its interaction with trailing edge can result in significant improvement in the efficiency of the system. Similar model of a tethered undersea kite was studied by Ghasemi et al. (2016) for power generation. In other fully passive systems, pitch and heave motions of the foil are independent of each other and oscillation amplitudes are controlled using linear and rotational springs and dampers (e.g. Peng and Zhu (2009), Zhu (2012)). For a hyper elastic body in a fluid stream, the solid body can also be treated as a highly viscous fluid to capture the interface between the two mediums (Esmailzadeh and Passandideh-Fard (2014)). For solving interface models, recent techniques include Phase field modeling, level set method and meshless hybrid methods. The phase field method substitutes a partial differential equation in place of a solid boundary condition in the form of a diffusion equation as demonstrated by Jacqmin (1999). The level set method can also be used for the analysis of curved shapes in a moving domain. Sussman and Puckett (2000) carried out an analysis of the motion of an inviscid air bubble in water through level set method.

In this study, the performance of semi-passive flapping foil systems is studied at various Reynolds numbers. The energy harvesting system comprises of an airfoil which is supported by a spring and damper system along its heave axis. The airfoil is subjected to sinusoidal pitch oscillation, about its elastic axis, through external activation. As a result of pitch oscillations, time varying fluid forces are subjected to airfoil surface which initiate oscillations in heave mode. Energy is extracted through heaving motion. Figure 1 shows the schematic of semi-passive system used here.

Numerical simulations are carried out on the hybrid fluid mesh using a coupled mesh based and meshfree solution scheme as suggested by Javed et al. (2014). The meshfree nodal cloud eliminates the need of re-meshing as it moves and adapts with the moving solid boundary. The Cartesian grid, enclosing the meshfree cloud, offers a computational efficient model in this hybrid scheme. The movable meshfree nodes are solved using the flow equations in the Arbitrary-Lagrangian-Eulerian (ALE) form.
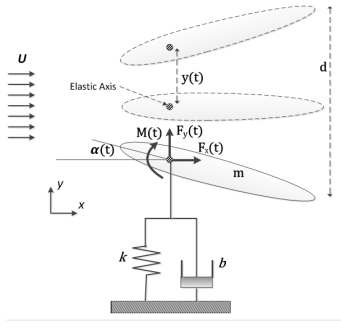
Fig. 1. Schematic of Pitching motion activated flapping foil

Fig. 2. Schematic of hybrid fluid grid around flapping airfoil

On the other hand, Cartesian grid is kept static and flow equations are solved in Eulerian formulation. A detailed layout of such a hybrid grid encompassing the airfoil is shown in Fig. 2. The Hybrid scheme based on meshfree RBF and Cartesian finite difference methods was presented by Javed et al. (2013), Javed et al. (2014) and Javed et al. (2016). The method benefits from the advantages of both meshfree and mesh based method. Meshfree method offers flexibility in dealing with moving boundaries and conventional finite differencing provides improved computational performance during the solution. The scheme is now extended for flapping foil flow energy harvesting problems at relatively higher Reynolds numbers.

At high Reynolds numbers, it is an established fact that convection becomes a significant factor in the solution. Numerical solution at these conditions may experience errors and instabilities caused by spurious fluctuations in the resultant parameters. The use of a stabilization technique is therefore, necessary at high Reynolds numbers. In this work, stabilization term suggested by Oñate (1998) has been used with flow momentum equation to avoid instabilities at high *Re* flow. The solutions are run for semi-passive system with NACA0015 airfoil at four different Reynolds numbers (Re = 5000, 10000, 20000 and 50000). The vortex structure, variation of aerodynamic parameters and performance of the system has been compared at different Reynolds numbers. Moreover, the effects of changing stiffness of translational spring, pitch amplitude and pitch frequency are studied at various Reynolds number.

2. PROBLEM FORMULATION

2.1 Problem Description

We consider the airfoil with mass *m* and chord length *c*. The airfoil is mounted on a translational spring with stiffness *k* and damper with damping constant *b* at its elastic axis as shown in Fig. 1. Airfoil is subjected to a sinusoidal pitching motion
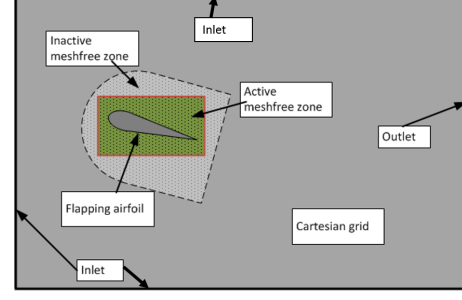
with frequency *f* amplitude θ_0 through an external drive. The pitching motion is therefore prescribed by the following equation:

$$\theta(t) = \theta_0 \sin(2\pi f t) \tag{1}$$

where $\theta(t)$ is the instantaneous pitch angle at time *t*. The externally activated pitch oscillation produces time varying fluid forces on the airfoil surface. As a result, plunging airfoil motion is induced. If $F_y(t)$ is instantaneous vertical force, exerted by the flow on the airfoil, the equation of motion for vertical translation is written as:

$$m\ddot{y} + b\dot{y} + ky = F_y(t) \tag{2}$$

External force $F_y(t)$ can be evaluated by integrating fluid stresses over the entire solid surface. The parameters appearing in Eqs. (1) and (2) can be non-dimensionalized using chord length (c), density of fluid (ρ) and free-stream velocity (U) as shown below:

$$t^* = \frac{tU}{c}, \qquad f^* = \frac{fc}{U}, \qquad y^* = \frac{y}{c}, \qquad C_y = \frac{F_y}{0.5\rho U^2 c}$$

$$m^* = \frac{m}{0.5\rho c^2}, \qquad b^* = \frac{b}{0.5\rho U c}, \qquad k^* = \frac{k}{0.5\rho U^2}$$

Corresponding non-dimensionalized governing equations are:

$$\theta(t) = \theta_0 \sin(2\pi f^* t^*) \tag{3}$$

$$m^* \ddot{y}^* + b^* \dot{y}^* + k^* y^* = C_y(t) \tag{4}$$

To acquire the heave displacements at subsequent time steps, explicit RK-4 method is utilized to the differential equations for motion of solid.

3

2.2 Net Extracted Power by Heave and Oscillating Airfoil modes

As depicted in Fig. 1, the airfoil is subjected to simultaneous pitch and heave motion. When the depth for the wing was considered as unity, Kinsey and Dumas (2008) presented the mathematical relations for the power extracted in both modes, as follows:

$$Heave\ Power = P_y(t) = y(t)V_y(t) \qquad (5)$$

$$Pitch\ Power = P_\theta(t) = \omega(t)M(t) \qquad (6)$$

where $M(t)$, $V_y(t)$, $y(t)$ and $\omega(t)$ are pitching moment, heave velocity, translational displacement and angular velocity respectively. The net extracted power is written as:

$$Net\ extracted\ power = P(t) = P_y(t) + P_\theta(t) \qquad (7)$$

The non-dimensionalized form of net extracted power is called as coefficient of power (C_{op}) and is written as:

$$C_{op} = \frac{P}{1/2\rho U^3 c} \qquad (8)$$

The extracted power can be integrated over time to obtain the mean power extracted over a complete cycle . Moreover, coefficient of extracted power can also be expressed in term of power related to pitching and heaving motions. Net coefficient of power over complete time oscillation ($\bar{C}_{op}$) can therefore, be written as:

$$\bar{C}_{op} = \bar{C}_{op_y} + \bar{C}_{op_\theta} \qquad (9)$$

$$\bar{C}_{op} = \frac{1}{T}\int \left(C_y(t)\frac{V_y(t)}{U} + C_M(t)\frac{\omega(t)c}{U} \right) dt \qquad (10)$$

where T is the time period of oscillation. Finally, the efficiency of extracted power η is stated in terms of available and extracted power:

$$\eta = \frac{P}{P_a} = \frac{P_y + P_\theta}{1/2\rho U^3 d} = \bar{C}_{op}\frac{c}{d} \qquad (11)$$

where d is the overall extent of airfoil vertical displacement as shown in Fig. 1.

2.3 Hybrid Fluid Grid

The Cartesian grid and meshfree nodal region form a hybrid grid in the complete domain, whose schematic around the airfoil is depicted in Fig. 2. The body conformal meshfree nodal region encompassing the airfoil forms the near field region, . A
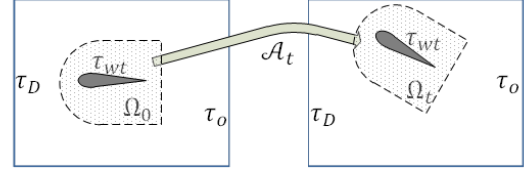

Fig. 3. ALE mapping of initial configuration Ω_0 over current configuration Ω_t

static Cartesian mesh is generated in the far field which surrounds and partially overlaps the meshfree nodes. A detailed discussion on treatment of meshfree and Cartesian nodes, activation / deactivation process and data transfer between the nodal zones can be envisioned in the research of Javed et al. (2014) and Javed et al. (2016).

2.4 Flow Equations

Airfoil movement occurs within in the dynamic meshfree zone which is achieved through the solution of flow equations in Arbitrary-Lagrangian-Eulerian (ALE) frame . Let Ω_0 be the initial configuration of computational domain as shown in Fig. 3. Using ALE method, this reference configuration Ω_0 can be mapped over current configuration Ω_t at any instant in time t as described by Hirt et al. (1974):

$$\mathcal{A}_t : \Omega_0 \rightarrow \Omega_t, \qquad \mathbf{X} \rightarrow x(\mathbf{X},t) = \mathcal{A}_t(\mathbf{X}) \qquad (12)$$

with ALE velocity calculated as $\mathsf{v} = \partial \mathcal{A}_t/\partial t$. At any spatial location in the domain, ALE velocity matches that of the computational node. In any current configuration Ω_t, the velocity-pressure $(P,\mathbf{u})$ formulation of time varying, viscous, incompressible N-S equations in non-dimensionalized ALE formulation is written as (Takashi and Hughes (1992)):

$$\partial_t \mathbf{u} = -\nabla P - (\mathbf{u} - \mathsf{v}).(\nabla \mathbf{u}) + (1/\mathbf{Re})\nabla^2 \mathbf{u} \qquad (13)$$

$$\nabla.\mathbf{u} = 0 \qquad (14)$$

On stationary (Cartesian) grid, the nodal velocity becomes zero ($\mathsf{v} = 0$). Therefore, Eulerian form of the momentum Eq. (13) is obtained (Takashi and Hughes (1992)). Pressure projection method based on Chorin algorithm (Chorin (1973)) is used here for pressure-velocity decoupling. Time discretization of Convective term is carried out using Adam-Bashforth scheme whereas Crank-Nicholson scheme is used for viscous term, as used by Kim and Moin (1985). In the meshfree zone, the space derivatives are treated with local RBFs in finite difference mode (RBF-FD). Detailed solution strategy and time marching scheme

4

in the meshfree and Cartesian zone is discussed in the work of Javed et al. (2014) and Javed et al. (2016).

2.5 Stabilization at High Reynolds Number

At higher Reynolds numbers, convection becomes a significant factor in the flow. In current work, the solutions are obtained at flow Reynolds numbers as high as 50,000. To avoid instabilities at such conditions, the use of a stabilization technique becomes vital. Use of anisotropic balancing diffusion, streamline upwind Petrove-Galerkin (SUPG) method (Brooks and Hughes (1982)) and Upwind finite differencing (Hirsch (2002)) are commonly used stabilization techniques. Oñate (1998) presented the concept of artificial or balancing diffusion for stabilizing the numerical solution of flow equations. They remarked that through standard conservation principles, at the time of derivation of these equations with higher order approximations, the stabilization term appears inherently from within the governing differential equations. Applicability of this technique has also been demonstrated for finite point method (FPM) by Oñate et al. (1996). Therefore, same technique is used here for stabilizing the flow solutions. Modified momentum equation with stabilized term, derived by Oñate (1998) is written as:

$$\frac{\partial \mathbf{u}}{\partial t} = -\mathbf{u}.\nabla \mathbf{u} - \nabla P + \frac{1}{Re}\nabla^2 \mathbf{u} - \frac{\Delta s}{2|\mathbf{u}|}\mathbf{u}^T.\nabla \mathbf{g}(\mathbf{u}) \tag{15}$$

$$(\text{where} \quad \mathbf{g}(\phi) = -\mathbf{u}.\nabla\phi - \nabla P)$$

Equation 15 is the flow momentum equation for incompressible viscous flow with an additional term $-\Delta s/(2|\mathbf{u}|)\mathbf{u}^T.\nabla \mathbf{g}(\mathbf{u})$ which stabilizing the solution. Stabilization is applied at the characteristic length Δs, which defines the size of finite domain. The value of this characteristic length is a function of Peclet Number (Pe). The characteristic length Δs is as:

$$Pe = \frac{|\mathbf{u}|\Delta \bar{s} Re}{2} \tag{16}$$

$$\alpha = \coth|Pe| - \frac{1}{|Pe|} \tag{17}$$

$$\Delta s = \alpha \Delta \bar{s} \tag{18}$$

In a hybrid grid, the value of $\Delta \bar{s}$ is defined separately in Cartesian and meshfree zones. In the Cartesian mesh, $\Delta \bar{s}$ is defined as the average space step at a particular point of interest. In the meshfree zone, $\Delta \bar{s}$ is the average distance represented by each node in any local influence domain and is expressed as $\Delta \bar{s} = 2r/N$ for any influence domain of N adjacent points with radius r. The control parameter (α)
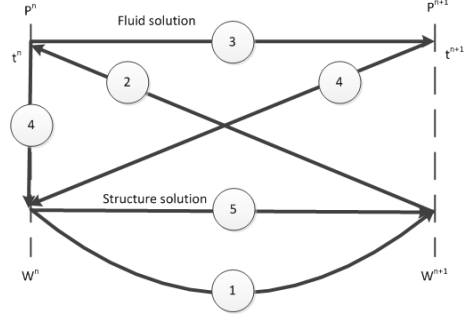

Fig. 4. Arbitrary-Lagrangian-Eulerian mapping of initial configuration Ω_0 over current configuration Ω_t

has a value of $0-1$ as the free stream velocity goes from $0-\infty$. In order to achieve higher stabilization in the regions with higher free stream velocities and higher convection rates, the value of characteristic length is controlled through this methodology.

2.6 Fluid-Solid Coupling

In this work, partitioned method has been used for fluid structure interaction. Coupling at fluid-solid interface has been achieved by a sub-iteration algorithm which attempts to reach convergence between fluid and structure solvers before moving on to the next time step iteration. A closed coupling is therefore ensured at interface boundary. Coupling algorithm for two-field solution, as shown in Fig. 4, proceeds by first predicting the solid displacements (W^{n+1}) using velocity and acceleration of previous time step. The airfoil and surrounding meshfree nodal cloud are displaced according to predicted solid displacement W^{n+1}. The fluid solution is then run with updated position of solid boundary and meshfree nodes. As a result, updated values fluid forces (P^{n+1}) are obtained at solid boundary. Effective loads on solid are calculated as an average of P^n and P^{n+1}. Subsequently, structural equations are solved to get corrected solid deflection W^{n+1}. These values are compared with previously obtained solid deflection values. The process is repeated until the solid deflection values (W^{n+1}) converge. A similar concept of time dependent update of displacement values from fluid forces is described by Elahi et al. (2015).

3. VALIDATION TEST CASES

3.1 Validation over Static Airfoils

The proposed solution scheme is validated by solving the flow around static NACA0012 airfoil at $Re10,000$ and $Re50,000$ respectively. As a first step, grid independence check is carried out to make sure that the accuracy of the solutions are independent of the nodal density. At each Reynolds
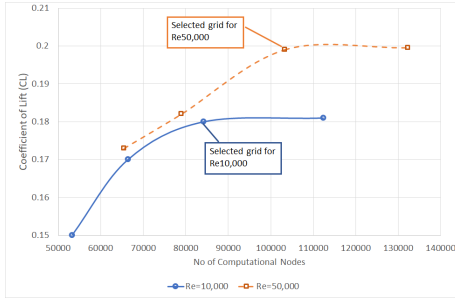
Fig. 5. Grid independence check carried out at $Re10,000$ and $Re50,000$ at $AoA = 5\ deg$ for NACA0012

number, the boundary layer thickness is calculated using empirical relation of laminar flow over a Blasius flat plate. The nodal distribution within the boundary layer is set by ensuring adequate nodal layers to guarantee the nodal resolution in the close vicinity of the airfoil. The flow parameters are set according to properties of air, with standard air density $\rho = 1.225 kg/m^3$ and dynamic viscosity $\mu = 1.8375 N.s/m^2$. The chord length for the airfoil is set as $c = 1.0m$. The Reynolds number yields the flow field velocity ($U = \mu Re/(\rho c)$). Boundary conditions are set as described in Section 2.4. A constant time step of 5.0×10^{-4} is used in all cases. Grid independence check is carried out at an angle of attack of 5 degrees. The solutions are run by progressively refining the nodal density. The values of coefficient of lift obtained for various grid sizes are plotted against the corresponding number of grid nodes in Fig. 5. The screenshots of selected grids for $Re = 10,000$ and $Re = 50,000$ are shown in Fig. 6(a) and 6(b) respectively.

Cases for static solutions are solved for multiple angles of attack ranging in $0 \leq \alpha \leq 20$. Figures 7(a) and 7(b) represnet the root mean square (RMS) values of lift coefficient C_L for $Re = 10000$ and $Re = 50000$, respectively. The comparison of results at $Re = 10000$ is carried out with numerical study done by Akbari and Price (2003) along with the experimental research carried out by Alam et al. (2010). The solution at $Re = 50000$ is in agreement with the experimental work by Huang and Lee (1999) and Alam et al. (2010). The values for bound the cases are found to be consistent with the available literature.

3.2 Validation Over Oscillating Airfoil

After validating the solution over static airfoil, the verification tests are now carried out for flow around pitching and heaving airfoils. Solution are run for NACA0015 airfoil which oscillates about its elastic axis at $c/3$ from leading edge. The cases are solved at $Re = 1000$ and $Re = 1100$. At such
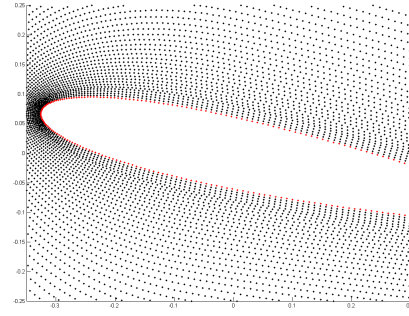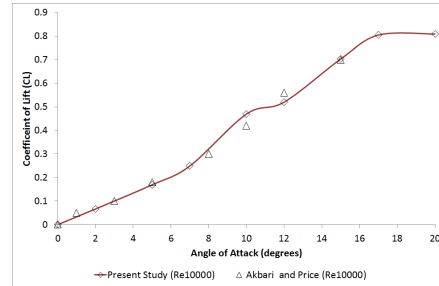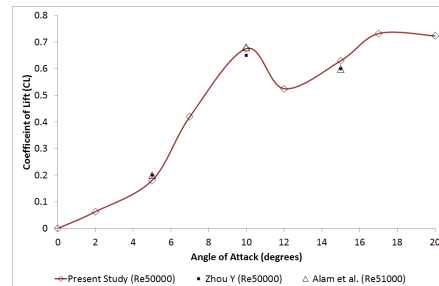

(a) Grid for 10000
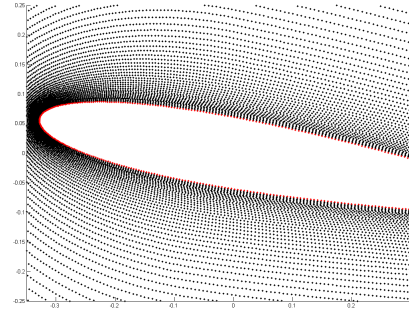
(b) Grid for $Re = 50,000$

Fig. 6. Modeled gird for multiple Reynolds numbers around NACA0012 airfoil

(a) $Re = 10000$

(b) $Re = 50,000$

Fig. 7. C_L vs α curves for multiple Reynolds number around NACA0012 airfoil
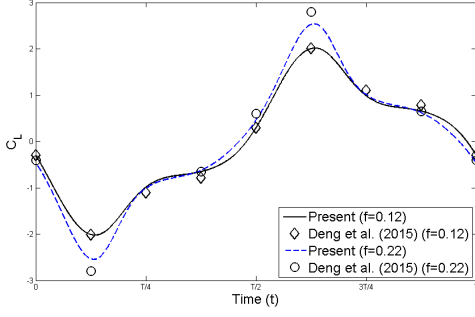
6

Fig. 8. Time-dependent variation of vertical force coefficient (C_y) for pitch-activated flapping NACA0015 airfoil during single oscillation period at $Re = 1000$, $\theta_0 = 75^o$, $k^* = 0$, $b^* = \pi, m^* = 0.1022$. Results compared with the solutions of Deng et al. (2015).

low Reynolds Numbers, laminar flow equations can easily be employed. The location of the airfoil is $4c$ from the inlet of the domain and $12c$ from outlet of the domain. Moreover, the width of domain is $10c$. The active meshfree zone around airfoil comprises of $1.35c \times 1.6c$ area. The airfoil surface is surrounded by 300 nodes in its vicinity. The complete computational domain consists of a total of 65354 conventional Cartesian nodes and 25880 meshfree nodes. Prescribed Pitching motion is imparted to the airfoil as per Eq. (3). Resulting heaving displacement is calculated by solving Eq. (4). Problem is solved using non-dimensionalized parameters. Heave reference frame is used to set up the problem. As a result, the dynamic mesh is not subjected to heave displacement. Although, there is an influence of heave velocity in the total net velocity of the dynamic nodes when formulating momentum equation in ALE formulation. The same methodology was employed by previous researchers (Kinsey and Dumas (2008), Wu et al. (2014) and Deng et al. (2015)) in their work. Four sets of mechanical parameters were considered for the simulations (θ_0, f^*, b^* k^*, m^*), and instantaneous values of force and moment coefficients are calculated over time. Subsequently, maximum values of vertical force coefficient (C_{ymax}), mean values of horizontal force coefficient (C_{xmean}) and maximum values of coefficient of moment (C_{Mmax}) are obtained during each oscillation period. These values are summarized in Table 1. The solutions are compared with the results obtained by Wu et al. (2014) and Deng et al. (2015) in their work. These solutions provide a good correlation with the available literature. The two test cases which were performed at $Re = 1000$; the comparison for the variation of C_y in the period of a single pitch oscillation is depicted in Fig. 8. It is noticed that as the frequency (f^*) increases, so does the peak value of vertical force. Time profiles

Table 1. Comparison of maximum values of vertical force coefficient (C_{ymax}), mean values of horizontal force coefficient (C_{xmean}) and maximum values of coefficient of moment (C_{Mmax}) for pitching-motion-activated-flapping NACA0015 airfoil

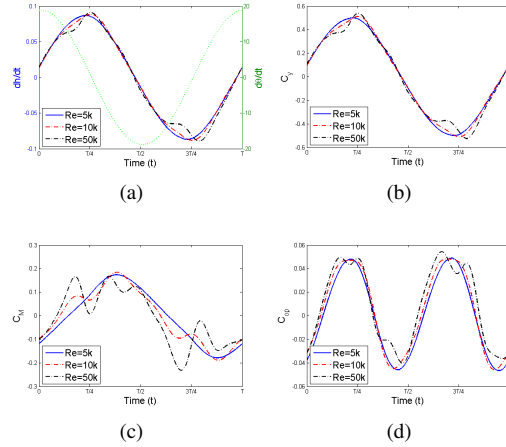| Source	C_{ymax}	C_{xmean}	C_{Mmax}
$Re = 1100$, $\theta_0 = 15^o$, $f^* = 0.2$, $f^* = 0.2$, $b^* = 2\pi$, $k^* = 10$, $m^* = 1$			
Wu et al. (2014)	0.704	0.179	-
Current study	0.69	0.17	-
$Re = 1100$, $\theta_0 = 30^o$, $f^* = 0.1$ $b^* = \pi$, $k^* = 0$, $m^* = 1$			
Wu et al. (2014)	0.905	0.345	
Current study	0.885	0.334	-
$Re = 1000$, $\theta_0 = 75^o$, $f^* = 0.12$, $b^* = \pi$, $k^* = 0$, $m^* = 0.1022$			
Deng et al. (2015)	2.0	-	0.33
Current study	2.017	-	0.31
$Re = 1000$, $\theta_0 = 75^o$, $f^* = 0.22$, $b^* = \pi$, $k^* = 0$, $m^* = 0.1022$			
Deng et al. (2015)	2.8	-	0.6
Current study	2.55	-	0.56

Fig. 9. Profiles of heave and pitch velocities (dh/dt and $d\theta/dt$), vertical force and moment coefficients (C_y, C_M) and coefficient of power (C_{op}) during a single oscillation period and at different Reynolds number for semi-passive flapping NACA0015 airfoil at $f^* = 0.2$, $k^* = 0$, $b^* = 2\pi$ and $\theta_0 = 15^o$

of vertical force are found to be in agreement with the results presented by Deng et al. (2015) in their work.

4. NUMERICAL TESTS

After validating the scheme for stationary and moving airfoil, test cases are run to determine the influence of translational stiffness (k^*), pitch frequen-
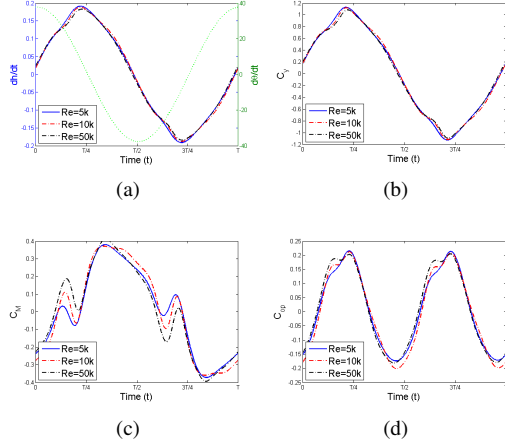
Fig. 10. Profiles of heave and pitch velocities (dh/dt and $d\theta/dt$), vertical force and moment coefficients (C_y, C_M) and coefficient of power (C_{op}) during a single oscillation period and at different Reynolds number for semi-passive flapping NACA0015 airfoil at $f^* = 0.2$, $k^* = 0$, $b^* = 2\pi$ and $\theta_0 = 30^o$

cies (f^*) and Reynolds number (Re) on system response and the effectiveness of power extraction of the semi-passive flapping foil energy extractor. For this purpose, test cases are solved for pitch frequencies in the range of $0.1 \le f^* \le 0.3$ and Reynolds numbers at $Re = 5000$, 10000, 20000 and 50000 for the same NACA0015 airfoil. Two different sets of results are obtained at $\theta_0 = 15^o$ and 30°, respectively. Influence of the variation in elastic stiffness is analyzed by carrying out calculations at three different values of non-dimensionalized stiffness ($k^* = 0$, 10 and 100). In all the test cases, the non-dimensionalized damping and mass constants are specified as $b^* = 2\pi$ and $m^* = 1$ and the location of the elastic axis is specified as $c/3$ from the leading edge of the airfoil.

4.1 Vortex Structure around Airfoil

The profiles of heave velocity (dh/dt), vertical force (C_y), moment coefficients (C_M) and coefficient of power (C_{op}), for $f^* = 0.2$, $k^* = 0$ and $\theta_0 = 15^o$ case, are plotted for a full oscillation cycle in Fig. 9. Instantaneous vorticity profiles around the airfoil, for the same case, at various stages of the periodic motion are shown in Fig. 11. During first quarter of oscillation period ($t < T/4$), the airfoil experiences pitch up motion from $\theta = 0 - \theta_0$. For $Re = 5000$ and 10000, a corresponding rise in vertical force (or lift), moment and heave velocity is observed during this period. Coefficient of power also rises from its minimum to maximum value due to increased lift. At higher Reynolds number ($Re = 50000$), vertical force profile experiences a

temporary slump, at $t \approx T/8$, before quickly recovering and peaking out at $t = T/4$. This transitory decline in the vertical force profile at $Re = 50000$ is due to re-attachment of leading edge separation vortex at airfoil lower surface close to the trailing edge, as shown in Fig. 11(a). The phenomenon is also demonstrated by corresponding decline in heave velocity and sudden rise in pitching moment at $t = T/8$. Subsequently, as the re-attached flow vortex leaves the trailing edge, lift is recovered and moment coefficient also reduces as shown in Fig. 11(b). At low Reynolds numbers such flow re-attachments are not observed because of insufficient inertial effects. After $t = T/4$, the airfoil starts its pitch down motion. During this phase, leading edge flow separation occurs at the upper surface of the airfoil. This separated flow has greater tendency to re-attach at downstream point at higher Reynolds numbers as shown in Fig. 11(c) and 11(d). For $Re = 50000$, the flow re-attachment results in lower pitching moments compared with $Re = 5000$ and 10000 cases. Consequently, less input power is needed and the coefficient of power momentarily rises during this period, for $Re = 50000$ case. From $t = T/2$ to $t = T$, flow parameters demonstrate similar behaviour in opposite direction.

Periodic variation of flow parameters and airfoil motion, for $\theta_0 = 30^o$ case, is shown in Fig. 10. Corresponding vortex profiles are shown in Fig. 12. An increase in the peak values of heave velocity, vertical force, moment and power is observed compared with the previous case. Moreover, Reynolds number has comparatively lesser effect on the system response. Leading edge vortex separation and subsequent re-attachment can also be seen at low Reynolds numbers now. Unlike $\theta_0 = 15^o$ case, no significant variation is observed in the qualitative response of the system with changing Reynolds number at $\theta_0 = 30^o$. However, the intensity of re-attached flow increases at high Re cases which correspondingly affects other parameters as shown in Fig. 10.

4.2 Effect of Changing Stiffness

The effect of stiffness of translational spring on the system response is studied by running the solutions for a three different values of stiffness ($k^* = 0$, $k^* = 10$ and $k^* = 100$). The resultant RMS values of vertical force $C_{y_{rms}}$), moment coefficients ($C_{M_{rms}}$ and mean of horizontal force coefficient ($C_{x_{mean}}$) are plotted against changing values of pitch frequency (f^*) at $Re = 5000$ in Fig. 13. It can be observed that force and moment coefficients increase with increasing stiffness values. Vertical force and moment coefficients initially reduce with increasing frequency (f^*) but later tend to increase. However, horizontal force coefficient monotonically reduces
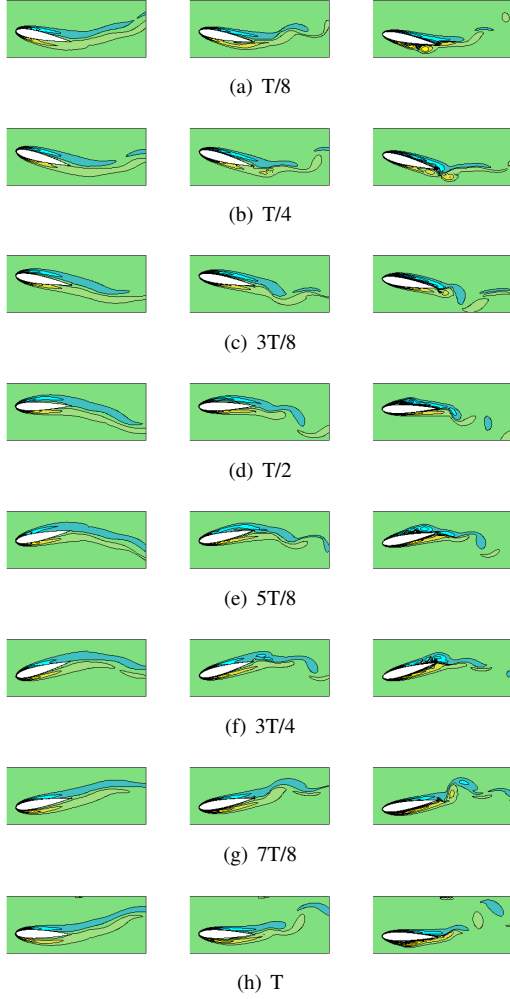
(a) T/8

(b) T/4
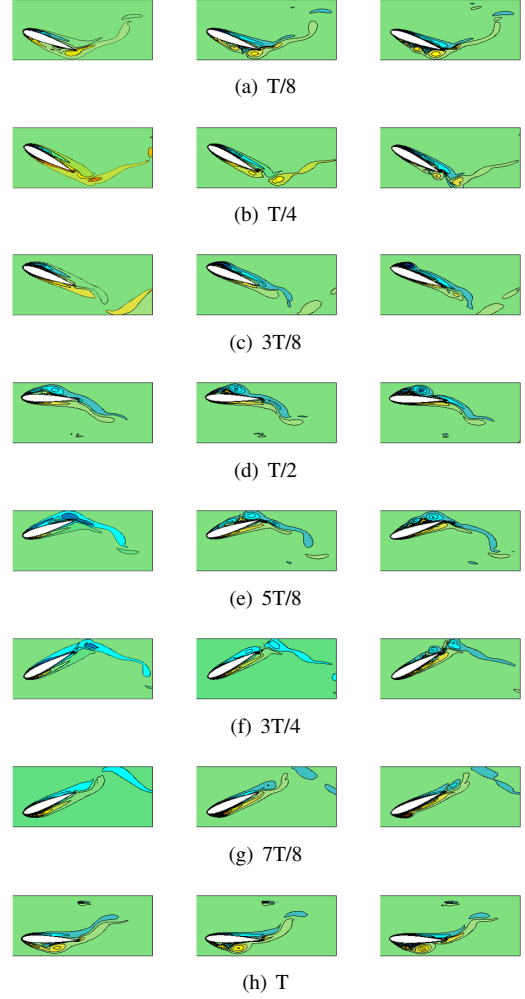
(c) 3T/8

(d) T/2

(e) 5T/8

(f) 3T/4

(g) 7T/8

(h) T

Fig. 11. Instantaneous vorticity profiles around pitch-activated flapping airfoil (NACA0015 at $k^* = 0$, $b^* = 2\pi$, $\theta_0 = 15^o$, $f^* = 0.2$). Lt column: $Re = 5000$, center column: $Re = 10000$, Rt column: $Re = 50000$

(a) T/8

(b) T/4

(c) 3T/8

(d) T/2

(e) 5T/8

(f) 3T/4

(g) 7T/8

(h) T

Fig. 12. Instantaneous vorticity profiles around pitch-activated flapping airfoil (NACA0015 at $k^* = 0$, $b^* = 2\pi$, $\theta_0 = 30^o$, $f^* = 0.2$). Lt column: $Re = 5000$, center column: $Re = 10000$, Rt column: $Re = 50000$

with increasing pitch rates.

Variation of overall extent of vertical displacement (d), net coefficient of power ($\bar{C}_{op}$) and power extraction efficiency (η) with changing pitch frequencies (f^*) have been shown in Figures 14 at $Re = 5000$. For $k^* = 10$, the vertical displacement initially increases with pitching frequencies and then stabilizes at constant level. However for $k^* = 0$, vertical displacement shows a declining trend with increasing pitch frequencies. Net coefficient of power and energy harvesting efficiency show reducing trends with increase in the values of f^*. Values of coefficient of power are significantly higher for $k^* = 0$ compared with $k^* = 10$. However, as vertical displacement is higher for $k^* = 0$, energy extraction efficiency reduces for this case. As a result, power extraction efficiencies, for $k^* = 0$ and $k^* = 10$ cases, are very close to each other. Net power

extraction generally remains negative at $k^* = 100$, which indicates that no energy can be extracted at this condition.

4.3 Effect of Changing Reynolds Number

The response of semi-passive flapping foil is now studied with changing Reynolds number. For this purpose, values of overall extent of vertical displacement (d), net coefficient of power ($\bar{C}_{op}$) and power extraction efficiency (η) are plotted with changing Reynolds numbers in Figures 15 and 16 for $\theta_0 = 15^o$ and 30°, respectively. The response curves have been obtained for $k^* = 0$ and for different values of f^*. At low pitching frequencies, net coefficient of power ($\bar{C}_{op}$) increases with increasing Reynolds numbers. However, the curves of $\bar{C}_{op}$ tend to level off at high Reynolds numbers. Moreover, sensitivity of $\bar{C}_{op}$ with Reynolds number re-
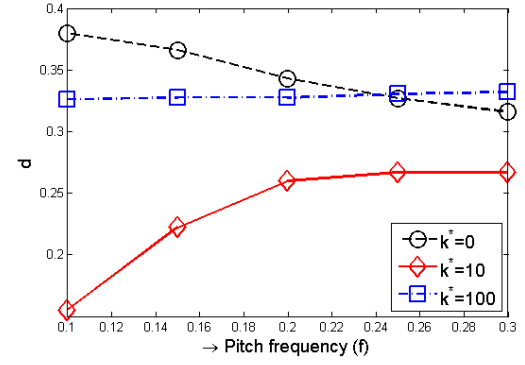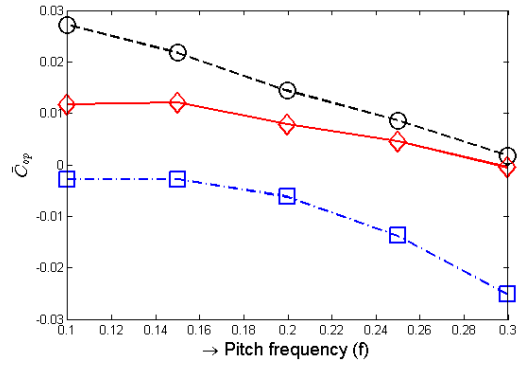
9
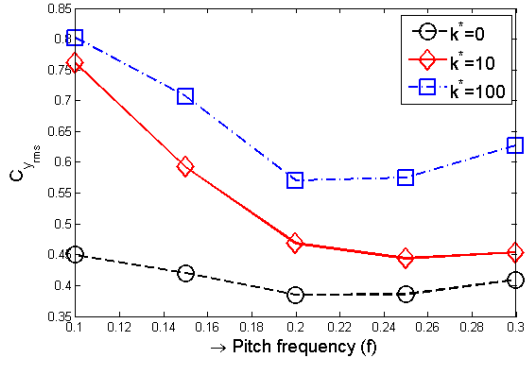
(a)
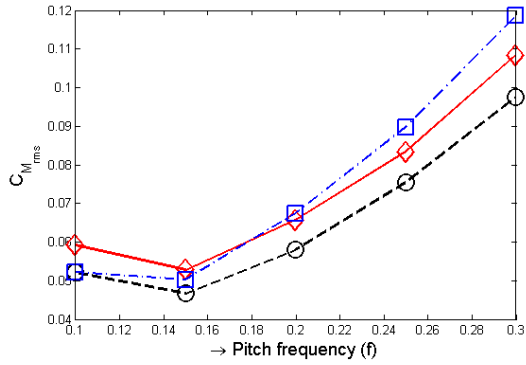
(b)
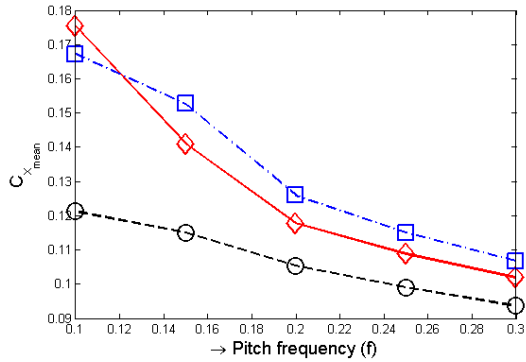
(c)

Fig. 13. Variation of RMS values of vertical force and moment coefficients ($C_{y_{rms}}$ and $C_{M_{rms}}$) and mean of horizontal force coefficient ($C_{x_{mean}}$) with changing pitch frequencies (f^*). Semi-passive flapping NACA0015 airfoil flow energy harvester at $Re = 5000$, $b^* = 2\pi$, $\theta_0 = 15^o$
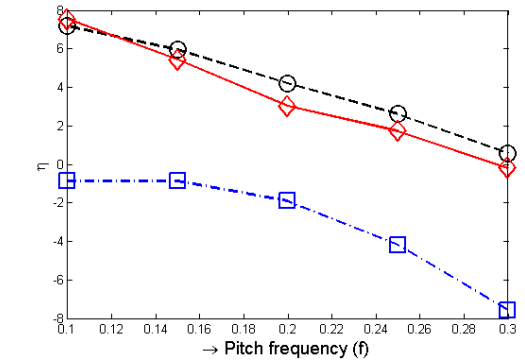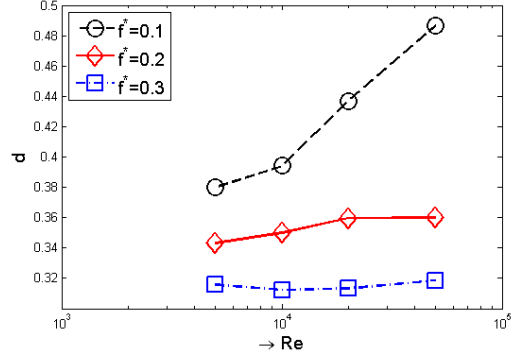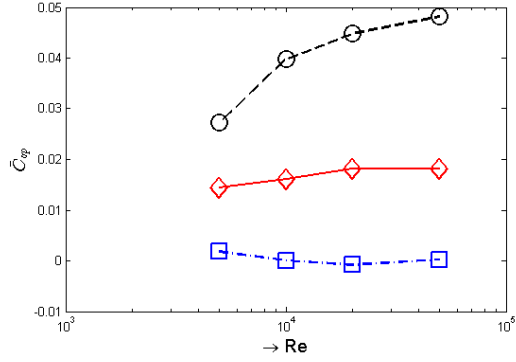

(a)

(b)

(c)

Fig. 14. Variation of overall extent of vertical displacement (d), net coefficient of power ($\bar{C}_{op}$) and power extraction efficiency (η) with changing pitch frequencies (f^*). Semi-passive flapping NACA0015 airfoil at $Re = 5000$, $b^* = 2\pi$, $\theta_0 = 15^o$

duces at higher pitching rates. Rising trend is also observed in the values of vertical displacement (d) with increasing Reynolds numbers. Within the domain of tested parameters, the power extracted from the flow is therefore, maximized at $f^* = 0.1$ and at $Re = 50000$. However, the efficiency values (η) suffer a decline at $Re = 50000$ due to higher amplitudes of translational vibration (d). The power

extraction also increases with increasing pitch amplitudes. For $\theta_0 = 30^o$, the power extraction efficiency reaches as high as 16% at $Re = 20000$. However, further increase in Reynolds number causes a reduction in the efficiency due to higher values of d.
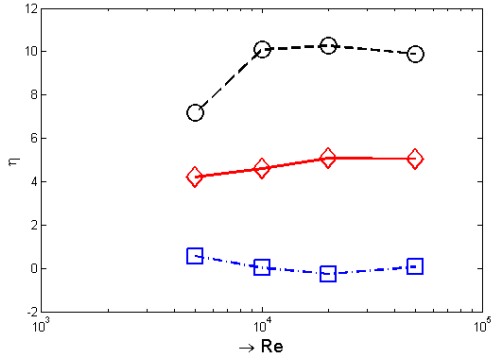
As the values of extracted power are found to be higher at $f^* = 0.1$, the system response is further investigated by varying the stiffness values (k^*) at
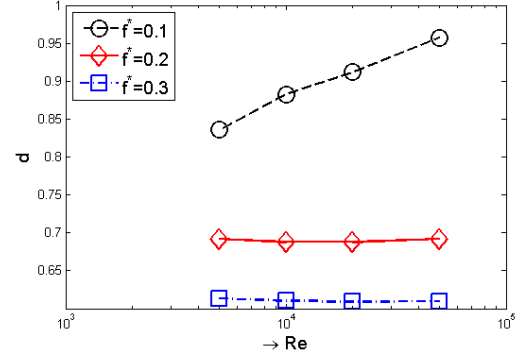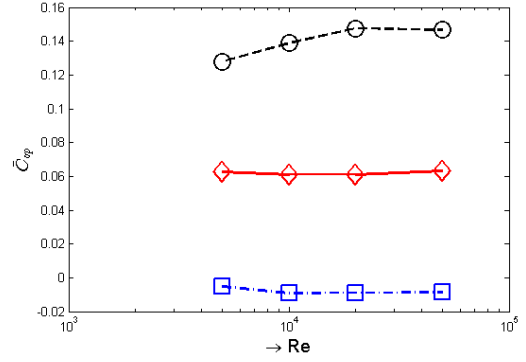
10

Fig. 15. Variation of overall extent of vertical displacement (d), net coefficient of power ($\bar{C}_{op}$) and power extraction efficiency (η) with changing Reynolds numbers (Re). Semi-passive flapping NACA0015 airfoil at $k^* = 0$, $b^* = 2\pi$, $\theta_0 = 15^o$

Fig. 16. Variation of overall extent of vertical displacement (d), net coefficient of power ($\bar{C}_{op}$) and power extraction efficiency (η) with changing Reynolds numbers (Re). Semi-passive flapping NACA0015 airfoil at $k^* = 0$, $b^* = 2\pi$, $\theta_0 = 30^o$
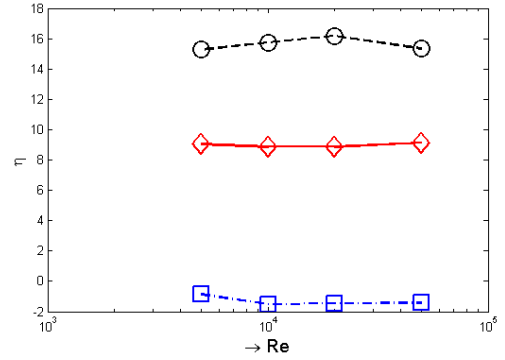
this frequency. Resultant plots are shown in Figures 17 and 18 for $\theta_0 = 15^o$ and 30°, respectively. It can be observed that coefficient of power shows an increasing trend with reducing the values of k^*. Figures 17(b) and 18(b) depict significant rise in the values of $\bar{C}_{op}$ when stiffness value (k^*) is reduced from 10 to 0. However, this gain in extracted power is not translated in the increased system efficiency (η) as shown in Figures 17(c) and 18(c). This is be-
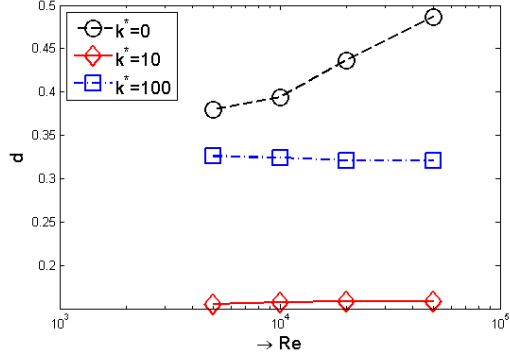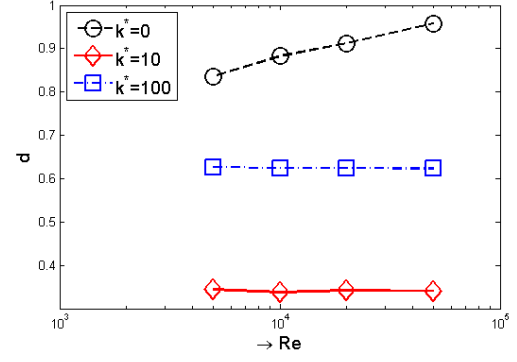
cause of the large increase in vertical displacement amplitude of airfoil from $k^* = 0 - 10$.
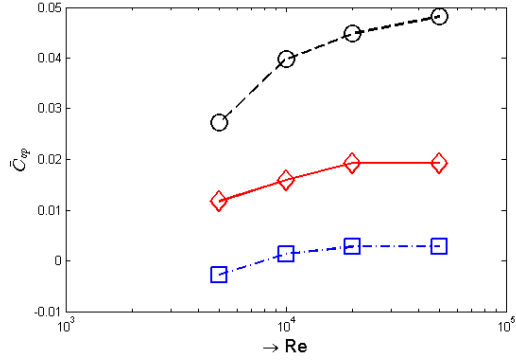
5. CONCLUSION

The application of hybrid meshfree-Cartesian grid scheme has been successfully demonstrated for semi-passive flapping foil flow energy harvesting problems. Instabilities at high Reynolds numbers were overcome by using stabilized flow momen-
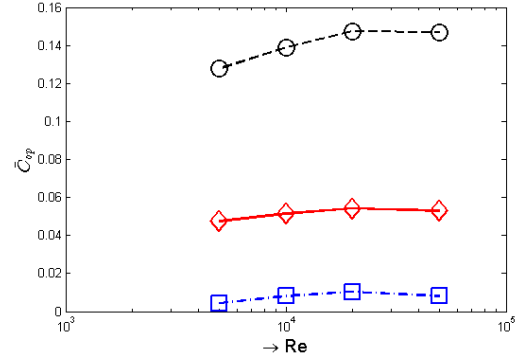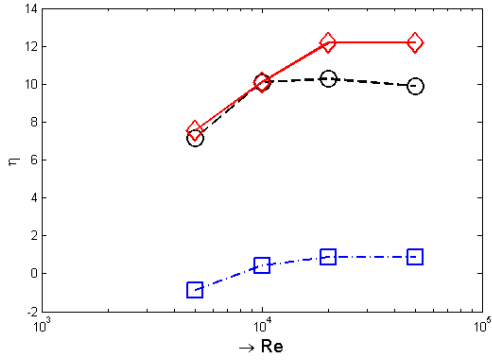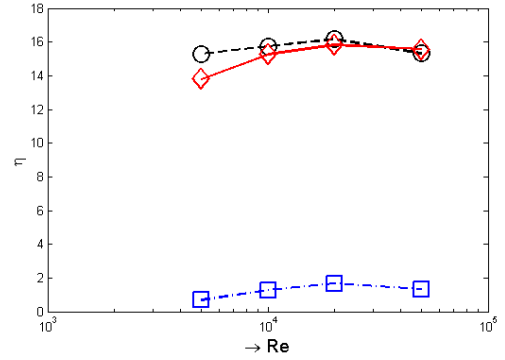
11

Fig. 17. Variation of overall extent of vertical displacement (d), net coefficient of power ($\bar{C}_{op}$) and power extraction efficiency (η) with changing Reynolds numbers (Re). Semi-passive flapping NACA0015 airfoil at $f^* = 0.1$, $b^* = 2\pi$, $\theta_0 = 15^o$

Fig. 18. Variation of overall extent of vertical displacement (d), net coefficient of power ($\bar{C}_{op}$) and power extraction efficiency (η) with changing Reynolds numbers (Re). Semi-passive flapping NACA0015 airfoil at $f^* = 0.1$, $b^* = 2\pi$, $\theta_0 = 30^o$

tum equations. The hybrid scheme offers flexibility to accommodate moving boundaries in a domain. With lesser computational requirements, this method offers potential applications for analysis of flexible objects as well. The need of re-meshing is eliminated by employment of this hybrid scheme as near field analysis is carried out within the mesh-free nodal cloud. The current scheme can provide insight into a semi-passive, shallow water movable

flap configuration which can be utilized for energy harvesting. The inner mesh free zone shares its nodal values with the underlying Cartesian grid, thus reducing the possibility of errors on the boundary of both zones. The accuracy of this method has been established in earlier research by Javed et al. (2013), Javed et al. (2014). The comparison of aerodynamic coefficients in Table 1 with those available in literature provides a reasonable accu-

racy. The accuracy test warrants the use of a same mesh size for subsequent test cases. The effects of variation in k, f and θ have been linked with the aerodynamic characteristics of moving flap. Furthermore, the study was extended to encompass the effects of changing Reynolds numbers.

At higher values of Reynolds numbers and pitch amplitudes, leading edge vortex separation and subsequent flow re-attachment was found to be a prominent feature which can affect the instantaneous performance of the system. At low Reynolds number flows, weaker tendency of separated flow to re-attach at downstream point can result in reduced coefficient of power. The overall qualitative behaviour of system response with changing pitch frequencies and translational stiffness remains unaffected by varying the Reynolds numbers. However, net coefficient of power and translational amplitudes tend to increase with increasing Reynolds numbers. This increase is more prominent at low pitch frequencies and smaller pitch amplitudes.

REFERENCES

Akbari, M. and S. Price (2003). Simulation of dynamic stall for a NACA 0012 airfoil using a vortex method. *Journal of Fluids and Structures 17*(6), 855–874.

Alam, M. M., Y. Zhou, H. Yang, H. Guo, and J. Mi (2010). The ultra-low Reynolds number airfoil wake. *Experiments in fluids 48*(1), 81–103.

Ashraf, M., J. Young, J. S. Lai, and M. Platzer (2011). Numerical analysis of an oscillating-wing wind and hydropower generator. *AIAA journal 49*(7), 1374–1386.

Boragno, C., R. Festa, and A. Mazzino (2012). Elastically bounded flapping wing for energy harvesting. *Applied Physics Letters 100*(25), 253906.

Brooks, A. N. and T. J. Hughes (1982). Streamline upwind/Petrov-Galerkin formulations for convection dominated flows with particular emphasis on the incompressible Navier-Stokes equations. *Computer Methods in Applied Mechanics and Engineering 32*(13), 199 – 259.

Chorin, A. J. (1973). Numerical study of slightly viscous flow. *Journal of Fluid Mechanics 57*, 785–796.

Deng, J., L. Teng, D. Pan, and X. Shao (2015). Inertial effects of the semi-passive flapping foil on its energy extraction efficiency. *Physics of Fluids (1994-present) 27*(5), 053103.

Elahi, R., M. Passandideh-Fard, and A. Javan-shir (2015). Simulation of liquid sloshing in 2d containers using the volume of fluid method. *Ocean Engineering 96*, 226–244.

Esmailzadeh, H. and M. Passandideh-Fard (2014). Numerical and experimental analysis of the fluid-structure interaction in presence of a hyperelastic body. *Journal of Fluids Engineering 136*(11), 111107.

Ghasemi, A., D. J. Olinger, and G. Tryggvason (2016). A nonlinear computational model of tethered underwater kites for power generation. *Journal of Fluids Engineering 138*(12), 121401.

Hirsch, C. (2002). *Numerical computation of internal and external flows*, Volume 2 of *Computational methods for inviscid and viscous flows*. Wiley-Interscience Publications.

Hirt, C., A. Amsden, and J. Cook (1974). An arbitrary Lagrangian-Eulerian computing method for all flow speeds. *Journal of Computational Physics 14*(3), 227–253.

Huang, R. F. and H. W. Lee (1999). Effects of freestream turbulence on wing-surface flow and aerodynamic performance. *Journal of aircraft 36*(6), 965–972.

Jacqmin, D. (1999). Calculation of two-phase navier–stokes flows using phase-field modeling. *Journal of Computational Physics 155*(1), 96–127.

Javed, A., K. Djidjeli, J. T. Xing, and S. Cox (2013). A hybrid meshfree local RBF- Cartesian FD scheme for incompressible flow around solid bodies. In A. Ariston (Ed.), *International Conference on Fluid Mechanics and Applications*. International Scientific Council.

Javed, A., K. Djidjeli, J. T. Xing, and Z. Sun (2014). *An ALE Based Hybrid Meshfree Local RBF-Cartesian FD scheme for Incompressible flow around moving boundaries*. AIAA Aviation. American Institute of Aeronautics and Astronautics. doi:10.2514/6.2014-2312.

Javed, A., K. Djijdeli, and T. Xing, Jing (2016). A coupled meshfree-mesh based solution scheme on hybrid grid for flow induced vibrations. *Acta Mechanica 227*(8), 2245–2274.

Jones, K. and M. Platzer (1997). Numerical computation of flapping-wing propulsion and power extraction. *AIAA paper 97*, 0826.

Kim, J. and P. Moin (1985). Application of a fractional-step method to incompressible Navier-Stokes equations. *Journal of Computational Physics 59*(2), 308–323.

Kinsey, T. and G. Dumas (2008). Parametric study of an oscillating airfoil in a power-extraction regime. *AIAA journal 46*(6), 1318–1330.

McKinney, W. and J. DeLaurier (1981). Wingmill: an oscillating-wing windmill. *Journal of energy 5*(2), 109–115.

Mirzaii, I. and M. Passandideh-Fard (2012). Modeling free surface flows in presence of an arbitrary moving object. *International Journal of Multiphase Flow 39*(Supplement C), 216 – 226.

Oñate, E. (1998). Derivation of stabilized equations for numerical solution of advective-diffusive transport and fluid flow problems. *Computer Methods in Applied Mechanics and Engineering 151*(1), 233–265.

Oñate, E., S. Idelsohn, O. C. Zienkiewicz, R. L. Taylor, and C. Sacco (1996). A stabilized finite point method for analysis of fluid mechanics problems. *Computer Methods in Applied Mechanics and Engineering 139*(1-4), 315–346.

Peng, Z. and Q. Zhu (2009). Energy harvesting through flow-induced oscillations of a foil. *Physics of Fluids (1994-present) 21*(12), 123602.

Sussman, M. and E. G. Puckett (2000). A coupled level set and volume-of-fluid method for computing 3d and axisymmetric incompressible two-phase flows. *Journal of computational physics 162*(2), 301–337.

Takashi, N. and T. J. R. Hughes (1992). An arbitrary Lagrangian-Eulerian finite element method for interaction of fluid and a rigid body. *Computer Methods in Applied Mechanics and Engineering 95*(1), 115–138.

Wu, J., Y. Qiu, C. Shu, and N. Zhao (2014). Pitching-motion-activated flapping foil near solid walls for power extraction: A numerical investigation. *Physics of Fluids (1994-present) 26*(8), 083601.

Wu, J., J. Wu, F.-B. Tian, N. Zhao, and Y.-D. Li (2015). How a flexible tail improves the power extraction efficiency of a semi-activated flapping foil system: A numerical study. *Journal of Fluids and Structures 54*, 886–899.

Wu, T. Y. and A. T. Chwang (1975). Extraction of flow energy by fish and birds in a wavy stream. In *Swimming and flying in nature*, pp. 687–702. Springer.

Wu, T. Y. T. (1972). Extraction of flow energy by a wing oscillating in waves. *Journal of Ship Res 16*, 66–78.

Young, J., M. A. Ashraf, J. C. Lai, and M. F. Platzer (2013). Numerical simulation of fully passive flapping foil power generation. *AIAA journal 51*(11), 2727–2739.

Zhu, Q. (2011). Optimal frequency for flow energy harvesting of a flapping foil. *Journal of fluid mechanics 675*, 495–517.

Zhu, Q. (2012). Energy harvesting by a purely passive flapping foil from shear flows. *Journal of Fluids and Structures 34*, 157–169.

Zhu, Q., M. Haase, and C. H. Wu (2009). Modeling the capacity of a novel flow-energy harvester. *Applied Mathematical Modelling 33*(5), 2207–2217.

Zhu, Q. and Z. Peng (2009). Mode coupling and flow energy harvesting by a flapping foil. *Physics of Fluids (1994-present) 21*(3), 033601.